JOURNAL OF SPACECRAFT AND ROCKETS
Vol. 39, No. 3, May–June 2002

Numerical Analysis on Separation Dynamics of Strap-On Boosters in the Atmosphere

Seongjin Choi,* Chongam Kim,† and Oh-Hyun Rho‡
Seoul National University, Seoul 151-742, Republic of Korea
and
Jeong-joo Park§
Korea Aerospace Research Institute, Yusung 305-606, Republic of Korea

A numerical technique for simulating the separation dynamics of strap-on boosters jettisoned in the dense atmosphere is presented. Six-degree-of-freedom, rigid-body equations of motion are integrated into the three-dimensional unsteady Navier–Stokes solution procedure to determine the dynamic motions of strap-ons. An automated chimera overset grid technique is introduced to achieve maximum efficiency for multibody dynamic motion, and a domain division technique is implemented in order to reduce the computational cost required to find interpolation points in the chimera grids. The flow solver is validated by comparing the computed results around the Titan IV launch vehicle with experimental data. The complete analysis process is then applied to the H-II launch vehicle, a major rocket in Japan's space program, and the KSR-III sounding rocket, a three-stage vehicle being developed in Korea. From the analyses separation trajectories of strap-on boosters are predicted, and aerodynamic characteristics around the vehicles at each time interval are examined. And separation-impulse devices, generally introduced for safe separation of strap-ons, are properly modeled, and the guideline map of additional jettisoning force and moment for safe separation is presented.

Nomenclature

c	=	speed of sound, m/s
ds	=	displacement vector, m
$d\alpha$	=	angular displacement vector, rad
$\hat{E}, \hat{F}, \hat{G}$	=	flux vectors
$\bar{F}$	=	resultant force vector, N
Fx, Fy, Fz	=	scalar components of $\bar{F}$, $\boldsymbol{N}$
$\bar{h}$	=	angular momentum vector
hx, hy, hz	=	scalar components of $\bar{h}$, kg · m^2/s
Iij	=	moment of inertia, kg · m^2
$\bar{M}$	=	resultant moment vector about mass center, N · m
Mx, My, Mz	=	scalar components of $\bar{M}$, N · m
p	=	pressure, N/m^2
$\hat{Q}$	=	conservative variable vector
$\bar{v}$	=	velocity vector, m/s
γ	=	specific heat ratio
ρ	=	density, kg/m^3
$\bar{\tau}$	=	shear stress vector
$\bar{\omega}$	=	angular velocity vector, rad/s

Introduction

THE accurate simulation of separated bodies in the dense atmosphere has been of great interest for several years. One major application of this technology is the separation dynamics of boosters from the parent. The strap-on boosters have been used to increase the payload capabilities of rockets, and for the safe separation of boosters without catastrophic collision the separation dynamics of the spent strap-on bodies from the parent rocket should be analyzed in detail. Many researchers have investigated this field numerically or experimentally. Meakin and Suhs[1] of NASA Ames analyzed the solid rocket booster (SRB) separation of a space shuttle with a Navier–Stokes solver. In his research, however, a prescribed trajectory was used for the dynamic analysis of body motion. Lochan and Adimurthy[2] attempted to analyze the separation dynamics of strap-on boosters from the core rocket, but they used wind-tunnel simulation data for the measurement of aerodynamic forces. Lijewski and Suhs[3] developed an unsteady simulation technique for store separation from a delta wing. In addition, with regard to vehicles with strap-on boosters, Palmer and Buning[4] analyzed the flowfield around the Conestoga 1620 launch vehicle with six boosters. Similar analyses were carried out by Taylor et al.[5] and Azevedo and Moraes[6] for the Titan IV with two boosters and for the AVLS launch vehicle with four boosters, respectively. Their studies were, however, focused on steady-state aerodynamic analyses without considering the relative motion of boosters. In fact, only a few numerical investigations seem to be reported, especially for the aerodynamic-dynamic coupled analysis for the separation of strap-ons, although multistage launch vehicles with boosters are widely used for many years.

Thus the present paper is focused on developing an efficient aerodynamic-dynamic coupled numerical solver to simulate booster separation dynamics of multistage vehicles. Six-degree-of-freedom, rigid-body equations of motion are integrated into the three-dimensional unsteady Navier–Stokes solver. An automated chimera overset grid technique is introduced to achieve maximum efficiency for multibody dynamic motion, and a domain division technique is implemented in order to reduce the computational cost required to find donor cells in the chimera grids. The developed flow solver is validated by comparing the computed results around the Titan IV launch vehicle with experimental data. The complete analysis process is then applied to two vehicle models of H-II and KSR-III. H-II is a two-stage rocket with two solid strap-ons, which has been a major rocket in Japan's space program. KSR-III is a three-stage sounding rocket with two large strap-ons, which is now being developed in the Republic of Korea. The detailed geometry of vehicles is described in the following section of this paper. From these analyses trajectories of strap-on boosters during the separation stages are predicted, and aerodynamic characteristics around the vehicles

Received 12 June 2001; revision received 26 September 2001; accepted for publication 28 September 2001.

*Doctoral Candidate, Department of Aerospace Engineering, San56-1 Shinlimdong.
†Assistant Professor, Department of Aerospace Engineering, San56-1 Shinlimdong.
‡Professor, Department of Aerospace Engineering, San56-1 Shinlimdong. Senior Member AIAA.
§Senior Researcher, Aerospace Research Group, 52 Eoundong.

at each time interval are examined. For safe separation of boosters, some additional jettisoning forces and moments are generally introduced by the separation-impulse devices such as spring ejectors or retrorockets. In this paper these separation-impulse devices are properly modeled, and the guideline map of additional jettisoning force and moment for safe separation is presented.

Description of Vehicles

Both the H-II and the KSR-III investigated in the present paper have symmetric configurations with two strap-on boosters, and the details of the geometry are shown in Fig. 1. In the configuration of H-II, the strap-on boosters are much smaller than the core rocket in diameter and length. However, the core and strap-ons of KSR-III are about the same size in order to employ the same rocket engine in both components. Thus the interactions between the core rocket and boosters during the separation stages might be particularly important in KSR-III. The nozzles of the rockets are not considered in actual simulation assuming that their effects on the separation dynamics are not critical. Specifications of the weight of bodies, the positions of center of gravity, and separation-impulse devices for two vehicles are presented in Table 1. The core rocket has two connectors for each booster, and the boosters are separated by the aerodynamic forces, gravity, and additional jettisoning forces.

Numerical Methods

Solution Procedure

To simulate the separation dynamics of bodies in compressible flow regime, it is necessary to understand the transient flowfields on and around the bodies. The obtained aerodynamic forces including gravity effect cause the relative motion of boosters. That is, the trajectory of boosters is predicted by the solutions of six-degree-of-freedom equations of motion with aerodynamic forces from a flow solver. The solution procedure is summarized as follows: 1) generate the overset grids around the bodies at the initial time level; 2) obtain the aerodynamic forces on the body surface from the flow analysis routine; 3) convert the aerodynamic forces including gravity and other additional control forces into the force and moment components acting on the c.g. of the body; 4) solve the rigid-body equations of motion, and get the new position and velocity components of the body at a next time level; and 5) move the body grids, and interpolate flow information at fringe cells, and repeat the unsteady analysis routine of 2–5.

Table 1 Core rocket and booster characteristics

Characteristic	H-II	KSR-III
c.g. of core rocket	20.60 m from base line	4.66 m from base line
c.g. of booster	10.88 m from base line	3.42 m from base line
Weight of core rocket	120,000 kg	5,500 kg
Weight of booster	70,000 kg (fuel free; 11,000 kg)	4,600 kg (fuel free; 1,000 kg)
Location of ejector 1	20.80 m from base line	5.80 m from base line
Location of ejector 2	4.00 m from base line	1.00 m from base line

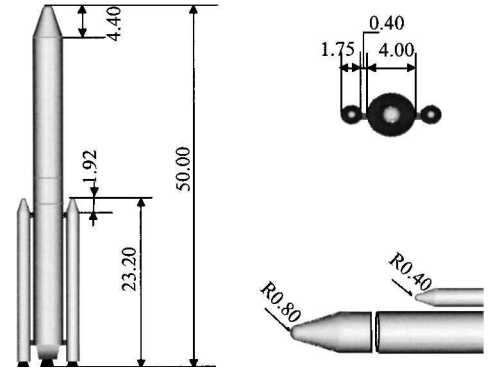

a) H-II

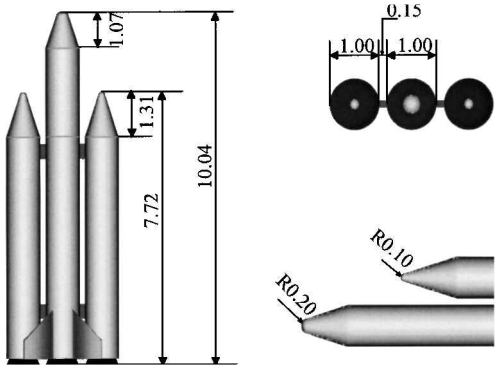

b) KSR-III

Fig. 1 Geometry.

Aerodynamic Analysis

Because the present vehicle does not contain massive flow separation regions except the base flow region whose effects are not considered in the present research, the three-dimensional compressible thin-layer Navier–Stokes equations are adopted for an efficient flow analysis. The thin-layer Navier–Stokes equations can be written in general curvilinear coordinates ξ, η, ζ as follows:

$$\frac{\partial \hat{Q}}{\partial t} + \frac{\partial \hat{E}}{\partial \xi} + \frac{\partial \hat{F}}{\partial \eta} + \frac{\partial \hat{G}}{\partial \zeta} = \frac{1}{Re}\frac{\partial \hat{G}_v}{\partial \zeta} \tag{1}$$

where

$$\hat{Q} = \frac{1}{J}\begin{bmatrix} \rho \\ \rho u \\ \rho v \\ \rho w \\ e \end{bmatrix}, \qquad \hat{E} = \frac{1}{J}\begin{bmatrix} \rho U \\ \rho u U + \xi_x p \\ \rho v U + \xi_y p \\ \rho w U + \xi_z p \\ (e+p)U - \xi_t p \end{bmatrix}$$

$$\hat{F} = \frac{1}{J}\begin{bmatrix} \rho V \\ \rho u V + \eta_x p \\ \rho v V + \eta_y p \\ \rho w V + \eta_z p \\ (e+p)V - \eta_t p \end{bmatrix}, \qquad \hat{G} = \frac{1}{J}\begin{bmatrix} \rho W \\ \rho u W + \zeta_x p \\ \rho v W + \zeta_y p \\ \rho w W + \zeta_z p \\ (e+p)W - \zeta_t p \end{bmatrix}$$

$$\hat{G}_v = \frac{1}{J}\begin{bmatrix} 0 \\ m_1 u_\zeta + m_2 \zeta_x \\ m_1 v_\zeta + m_2 \zeta_y \\ m_1 w_\zeta + m_2 \zeta_z \\ m_1 m_3 + (m_2/3)(\zeta_x u + \zeta_y v + \zeta_w w) \end{bmatrix}$$

with

$$m_1 = \mu\left(\zeta_x^2 + \zeta_y^2 + \zeta_z^2\right), \qquad m_2 = \mu\left(\zeta_x u_\zeta + \zeta_y v_\zeta + \zeta_z w_\zeta\right)$$

$$m_3 = \frac{\mu}{2}(u^2 + v^2 + w^2)_\zeta + \frac{\mu}{Pr}\frac{(c^2)_\zeta}{\gamma - 1}$$

and U, V, W are contravariant velocity components, which can be written as

$$U = \xi_x u + \xi_y v + \xi_z w, \qquad V = \eta_x u + \eta_y v + \eta_z w$$

$$W = \zeta_x u + \zeta_y v + \zeta_z w$$

In Eq. (1) the viscous terms involving velocity gradients in both ξ, η directions are neglected and in the normal direction ζ are collected into the vector $\hat{G}_v$. Turbulent viscous components are evaluated using the Baldwin–Lomax algebraic turbulence model[7] with a modified Degani–Schiff technique.[8]

For the temporal discretization of unsteady flowfield, dual time stepping is employed to obtain a second-order accuracy:

$$\frac{\partial \hat{Q}}{\partial \tau} = -\hat{R}^{n+1,s+1} - \frac{3\hat{Q}^{n+1,s+1} - 4\hat{Q}^n + \hat{Q}^{n-1}}{2\Delta t} \tag{2}$$

where

$$\hat{R} = \frac{\partial \hat{E}}{\partial \xi} + \frac{\partial \hat{F}}{\partial \eta} + \frac{\partial (\hat{G} - \hat{G}_v)}{\partial \zeta}$$

Here τ represents a pseudotime, n is the physical time level, and s is the pseudo time level. Equation (2) is discretized in pseudotime by the Euler implicit method and is linearized using the flux Jacobian. This leads to a large system of linear equations in delta form at each pseudo time step as

$$\left(\frac{I}{J\Delta\tau} + \left[\frac{\partial R}{\partial Q}\right] + \frac{1.5I}{J\Delta t}\right)\Delta Q = -R^{n+1,s} - \frac{3Q^{n+1,s} - 4Q^n + Q^{n-1}}{2J\Delta t} \tag{3}$$

The lower–upper symmetric Gauss–Seidel scheme[9] is used as the implicit time-integration method of Eq. (3). The viscous flux Jacobian is neglected in the implicit part because it does not influence a solution accuracy, and local time stepping is used.

As a spatial discretization, AUSMPW+ (modified advection upstream splitting method press-based weight function)[10] has been applied. AUSMPW+ is designed to remove the nonmonotone pressure solutions of the hybrid flux-splitting schemes such as AUSM and AUSM+ by introducing pressure weighting functions as a limiter at a cell interface.

For a higher-order spatial accuracy the monotone upstream-centered schemes for conservation laws[11] approach is used. Primitive variables are extrapolated at a cell interface, and the differentiable limiter[12] is employed to suppress unphysical oscillations near physical discontinuities.

Dynamic Analysis

The basic equations of rigid-body motion with respect to the coordinates XYZ attached to the core rocket (Fig. 2) are expressed as

$$\bar{F}_{cg} = \left(m\frac{d\bar{v}}{dt}\right)_{XYZ}, \qquad \bar{M}_{cg} = \left(\frac{d\bar{h}}{dt}\right)_{XYZ} \tag{4}$$

In these equations $\bar{v}, \bar{h}$ are velocity and angular momentum vector with respect to center of mass of the body, $\bar{F}_{cg}$, $\bar{M}_{cg}$ are external force and moment vector acting on the c.g. of the body, and they are represented as follows:

$$\bar{F}_{cg} = \bar{F}_{ad} + \bar{F}_{gv} + \bar{F}_{ct}, \qquad \bar{M}_{cg} = \bar{r}_0 \times (\bar{F}_{ad} + \bar{F}_{gv} + \bar{F}_{ct}) \tag{5}$$

Here $\bar{F}_{gv}$, $\bar{F}_{ct}$ represent gravity and additional control forces and the aerodynamic forces

$$\bar{F}_{ad} = \int_s (-p\hat{n} + \bar{\tau})\, dS \tag{6}$$

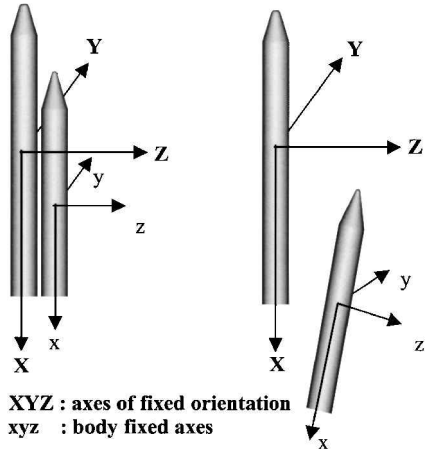

Fig. 2 Reference frames.

Because the moments and products of inertia of the body would change continually as a result of its rotation, it is necessary to determine their values as functions of time. It, therefore, is more convenient to use the coordinates xyz attached to the rotating booster as shown in Fig. 2, which ensures that its moments and products of inertia maintain the same values during the motion. Then, the moment equations relative to the moving coordinate system xyz with an angular velocity $\bar{\omega}$ become

$$\bar{M}_{cg} = \left(\frac{d\bar{h}}{dt}\right)_{xyz} + \bar{\omega} \times \bar{h} \tag{7}$$

Because the xyz axes coincide with the principal axes of inertia of the rotating body, the angular momentum $\bar{h}$ can be simplified as

$$h_x = \omega_x I_{xx}, \qquad h_y = \omega_y I_{yy}, \qquad h_z = \omega_z I_{zz} \tag{8}$$

Then the moment equations of motion are expressed as

$$\begin{aligned} M_x &= I_{xx}\dot{\omega}_x - (I_{yy} - I_{zz})\omega_y\omega_z \\ M_y &= I_{yy}\dot{\omega}_y - (I_{zz} - I_{xx})\omega_z\omega_x \\ M_z &= I_{zz}\dot{\omega}_z - (I_{xx} - I_{yy})\omega_x\omega_y \end{aligned} \tag{9}$$

which are usually referred to as the Euler's equations of motion. With the force relation of Eq. (4) in scalar form,

$$F_x = m\dot{v}_x, \qquad F_y = m\dot{v}_y, \qquad F_z = m\dot{v}_z \tag{10}$$

Equations (9) and (10) form a system of six differential equations and have a unique solution if initial conditions are given.

For the calculation of the equations of motion, the force equations are discretized in the inertial coordinate system (XYZ) directly, whereas moment equations are solved in the moving coordinate system (xyz). After computing the forces and moments the new velocity $\bar{v}^{n+1}$ and displacement ds^{n+1} are obtained by

$$\frac{\bar{v}^{n+1} - \bar{v}^n}{\Delta t} = \frac{1}{m}\bar{F}^n, \qquad ds^{n+1} = \frac{1}{2}(\bar{v}^n + \bar{v}^{n+1})\Delta t \tag{11}$$

and the new angular momentum $\bar{\omega}^{n+1}$ is calculated from Eq. (9) as

$$\begin{aligned} \frac{\omega_x^{n+1} - \omega_x^n}{\Delta t} &= \frac{1}{I_{xx}}[M_x + (I_{yy} - I_{zz})\omega_y\omega_z] \\ \frac{\omega_y^{n+1} - \omega_y^n}{\Delta t} &= \frac{1}{I_{yy}}[M_y + (I_{zz} - I_{xx})\omega_z\omega_x] \\ \frac{\omega_z^{n+1} - \omega_z^n}{\Delta t} &= \frac{1}{I_{zz}}[M_z + (I_{xx} - I_{yy})\omega_x\omega_y] \end{aligned} \tag{12}$$

Finally the angular displacement is updated as

$$d\alpha^{n+1} = \tfrac{1}{2}(\bar{\omega}^n + \bar{\omega}^{n+1})\Delta t \tag{13}$$

From the preceding dynamic analysis the new position and velocity components at a next time level are determined.

Grid Scheme

With moving body problems it is essential to have the initial grid distribution strictly adjusted to the motion of bodies. In this regard, unstructured grid techniques and overset grid techniques are known to be the most pertinent ones. Although the unstructured grid technique has a good flexibility in generating grids around complex geometry, all grids close to bodies should be carefully regenerated for any motion of bodies to maintain the quality of initial grids. The chimera overset grid technique can maintain high grid quality only by rotating or translating initial grids in those moving problems. Thus the chimera overset grid technique proposed by Steger et al.[13] is adopted in the present paper. For the efficient communication of conservative variables on the overset regions, the trilinear interpolation technique is introduced, and this is based on

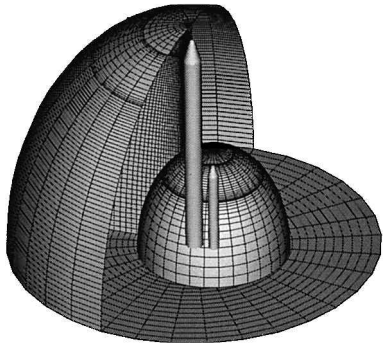

a) Initial stage

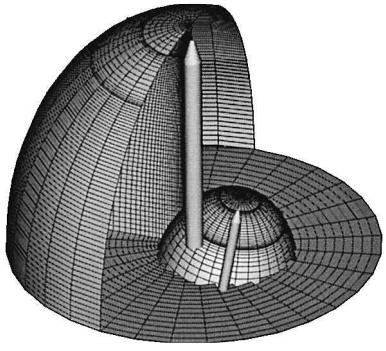

b) Moving stage

Fig. 3 Grid system.

the Newton–Raphson method in isoparametric coordinates. If any of the eight donor cells exists inside the hole region, the nearest cell around the donor in nonhole region is used as substitutes. With the trilinear interpolation it is very important to ensure that the grid distributions of the common, overlapping volume are not drastically different. Radical differences can lead to poor interpolation results.[14] Poor interpolation can in turn lead to increased computational time as a result of poor solution convergence. Therefore, in the present paper grid distributions of the overlapping volume are carefully treated to have good similarity.

In three-dimensional problem it generally takes much time to find the donor cells in the whole grid region. Especially for unsteady problems, this search should be repeated at every time interval, and it takes a considerable portion of the whole computation time. In the present paper, in order to reduce the searching time of donor cells in target domain, a simple domain division technique is introduced. In this technique, prior to finding the donor cells the target domain is divided into a number of subdomains. The subdomain including the fringe cell is then predetermined by simple comparison of position coordinates. This allows even faster searching in the determined subdomain. The core rocket grid and the booster grid generated by Gridgen V.13 are shown in Fig. 3a. One of the moving grids is shown in Fig. 3b.

Results and Discussion

Flow Solver Validation

As a validation of the developed flow solver, which directly influences the trajectory of vehicles, wind-tunnel data of the Titan IV launch vehicle are used.[5] The freestream Mach number is 1.6, and the Reynolds number is 1.1×10^7 with zero angle of attack. For the grid system overset grids of $101 \times 66 \times 121$ points for the core rocket and $81 \times 66 \times 101$ for the booster are used. Figure 4 shows the cross-sectional pressure contour of the Titan IV vehicle and Fig. 5 for the calculated surface pressure along the centerline of the vehicle compared with experimental wind-tunnel data. The close agreement between experimental and computed values can be observed in most regions except the connecting point of the core rocket and booster, where the computed values are a little underestimated because of the effect of a connecting cable in the wind-tunnel test.[5]

Table 2 Nondimensional aerodynamic forces and moment in the initial stage of separation

Vehicle	Cx	Cz	Cm
H-II	0.1161	0.0006	0.0065
KSR-III	0.5709	0.0070	−0.0577

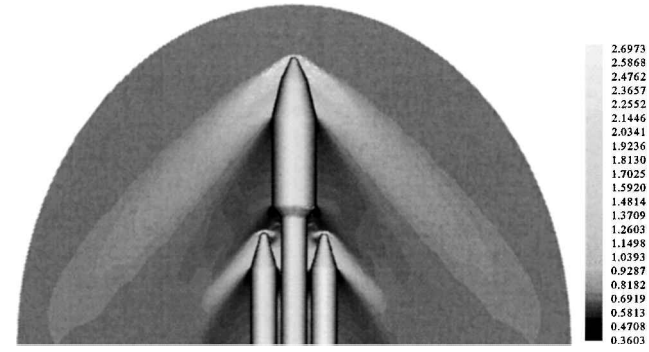

Fig. 4 Pressure contours around Titan IV launch vehicle (Mach = 1.6, angle of attack = 0 deg).

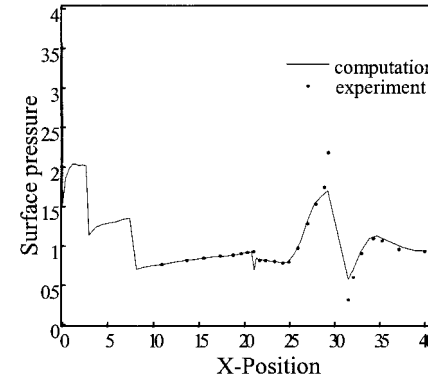

Fig. 5 Comparison of computed surface pressure with wind-tunnel data (along the centerline of the core rocket).

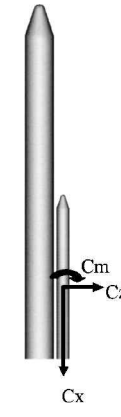

Fig. 6 Directions of nondimensional aerodynamic forces and moment.

Separation Dynamics of H-II

In this section the aerodynamic characteristics around the H-II vehicle at the initial stage of separation are first examined, and then simulations of separation dynamics are presented based on the initial stage results. The freestream Mach number is 2.0, and the Reynolds number is 9.0047×10^6, and $101 \times 66 \times 121$ grid points are used for the core rocket and $51 \times 66 \times 101$ for the booster.

Directions of the nondimensional axial force Cx, the normal force Cz, and the pitching moment Cm acting on the surface of the booster are defined as shown in Fig. 6. Pressure contours on and around the vehicle are shown in Fig. 7, and the nondimensional forces and moment are presented in Table 2. At the initial stage Cx is positive and produces the downward motion of booster mainly because of its weight. Cz and Cm are also positive values and makes the outward positive pitching motion of booster.

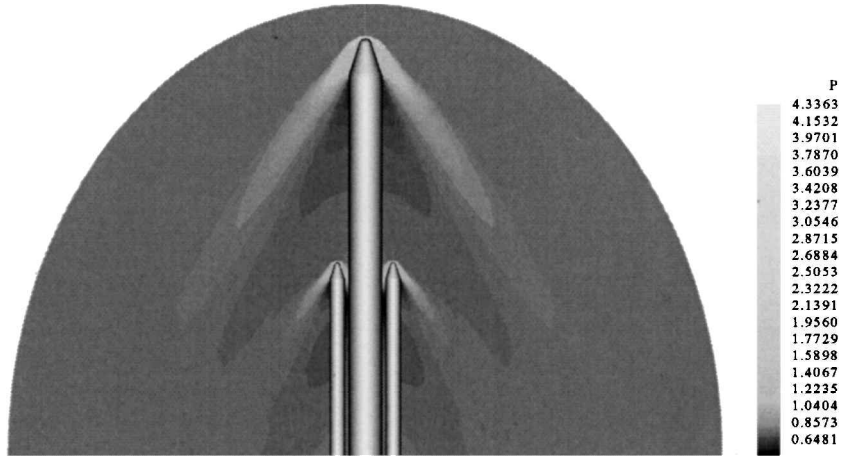

Fig. 7a Pressure contours around the H-II (initial stage, Mach = 2.0, $Re = 9.0047 \times 10^6$).

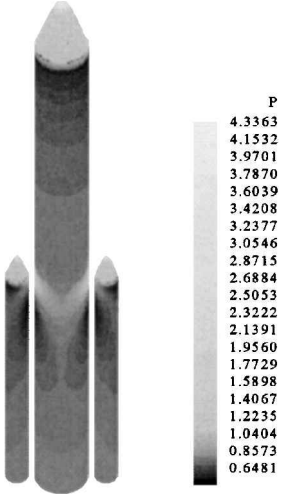

Fig. 7b Pressure contours on the surface of the H-II (initial stage, Mach = 2.0, $Re = 9.0047 \times 10^6$).

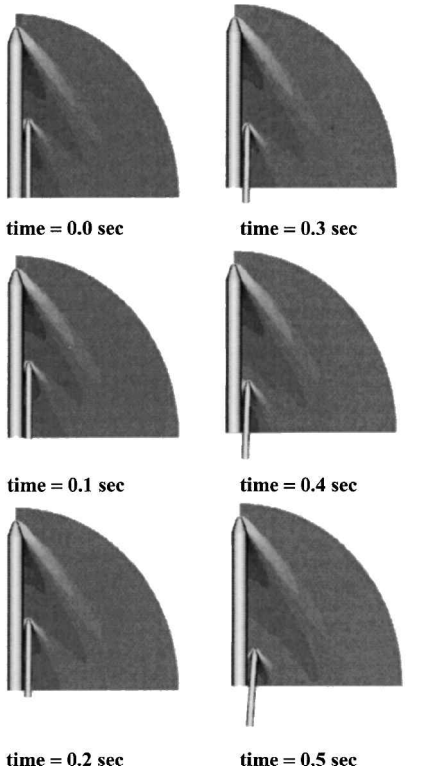

Fig. 8 Booster trajectory of H-II with pressure contours (free separation, no jettisoning force and moment).

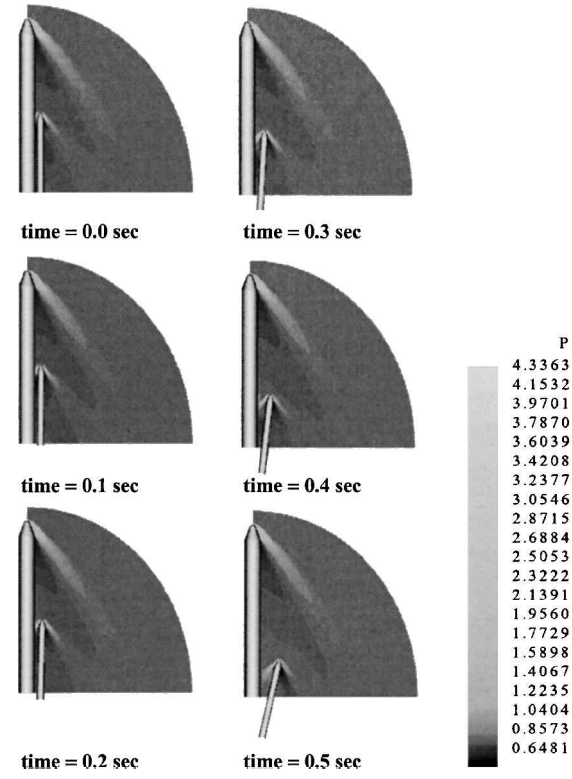

Fig. 9 Booster trajectory of H-II with pressure contours (nondimensional jettisoning force = 0.060, jettisoning moment = 0.030).

Separation dynamics of strap-on boosters is then simulated at the physical time step of 0.005 s. In this simulation the chimera overset moving grid scheme is used with the domain division technique. First, free body separation is simulated where the booster is simply released from the core rocket. From the design of H-II, the initial distance between the core rocket and booster is set to 0.4 m. As predicted from the initial stage analysis, the booster falls vertically with a small positive pitching motion as time evolves. In Fig. 8 the trajectory of booster and corresponding pressure contours around the bodies are shown at every 0.1 s after separation. In this simulation the booster seems to be quite close to the core rocket during all of the stages. Thus it would be better to introduce some additional jettisoning forces and moments using separation-impulse devices. The H-II uses the spring ejection systems as separation-impulse devices, and in the present paper their effects are replaced by the impact normal forces of different magnitude acting at the two connecting points for initial 0.005 s. Then a forced separation case is simulated with the nondimensional jettisoning force of 0.060 and moment of 0.030. Figure 9 shows the booster trajectory and pressure

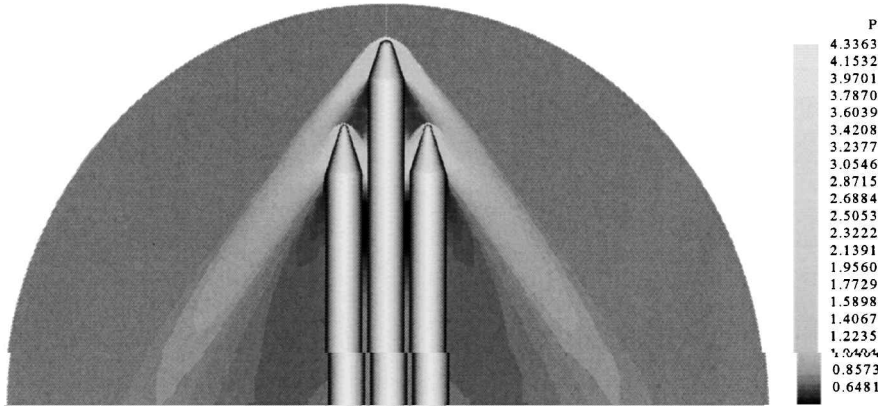

Fig. 10a Pressure contours around the KSR-III (initial stage, Mach = 2.0, $Re = 9.0047 \times 10^6$).

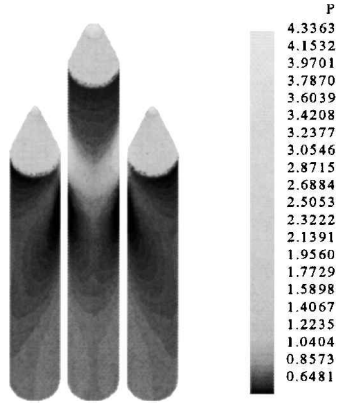

Fig. 10b Pressure contours on the surface of the KSR-III (initial stage, Mach = 2.0, $Re = 9.0047 \times 10^6$).

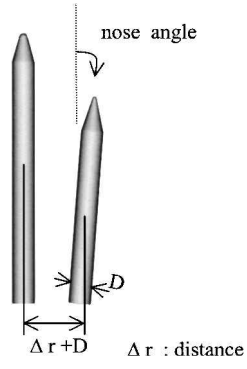

Fig. 11 Attitude definitions of booster.

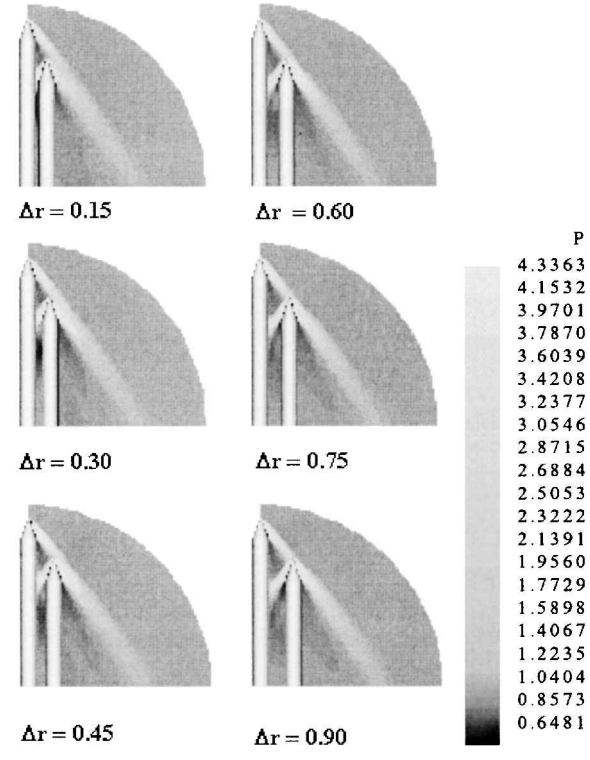

Fig. 12 Pressure contours at various distances of booster (Mach = 2.0, $Re = 9.0047 \times 10^6$).

contour around the vehicle in this simulation, and a safer separation is expected.

Separation Dynamics of KSR-III

In the same manner the aerodynamic characteristics of KSR-III at the initial stage of separation are examined, and the results are compared with those of H-II. Because the boosters are located near the nose/cylinder expansion region of the core at the initial stage, the flowfield characteristics of KSR-III are more complex. Thus some additional investigations are added to analyze the effects of expansion waves of the core on the booster. And at last, based on the results, simulations of separation dynamics are presented. Freestream Mach number is 2.0, and the Reynolds number is 9.0047×10^6. A $101 \times 66 \times 121$ grid is used for the core rocket and $81 \times 66 \times 101$ for the booster.

In Fig. 10 pressure contours on and around the vehicle at the initial stage are shown. The aerodynamic forces and moment are presented in Table 2. Comparing these aerodynamic characteristics with those of H-II, an interesting feature is found. The pitching moment Cm is a negative value, which is opposite to the result of H-II. Thus the booster trajectory of KSR-III in the separation stages might be also quite different from that of H-II.

This adverse aerodynamic feature seems to be from the expansion waves of the core rocket. Concerning this matter, some additional aerodynamic characteristics are examined at various attitudes of booster. As shown in Fig. 11, attitudes of booster are represented by two factors: the distance from the core rocket and the nose angle with respect to the core rocket. In Figs. 12 and 13 pressure contours around the vehicles at different distances and different nose angles are shown, respectively. In Fig. 14a the nondimensional aerodynamic forces and moment acting on the surface of booster are compared at various distances. In this figure variation of Cm is most remarkable, and it changes from a negative to positive value as the distance increases. Similarly in Fig. 14b, the aerodynamic forces are compared at various nose angles. Cz, Cm are both increasing as the nose angle increases, but Cx is nearly constant in all cases. The behaviors of Cz, Cm are believed to be caused by the expansion waves of the core rocket striking the nose of booster. From these results it might be said that an offset distance and positive nose angle of booster at the initial stage of separation are advantageous for an easy separation.

Based on the preceding aerodynamic results, separation dynamics of KSR-III is simulated at the physical time step of 0.005 s. In Fig. 15 the trajectory of booster and corresponding pressure contours

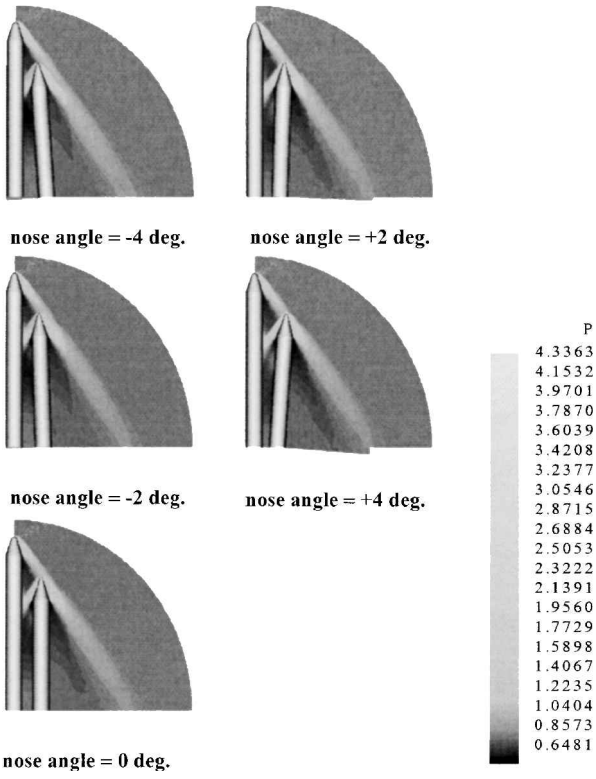

Fig. 13 Pressure contours at various nose angles of booster (Mach = 2.0, $Re = 9.0047 \times 10^6$).

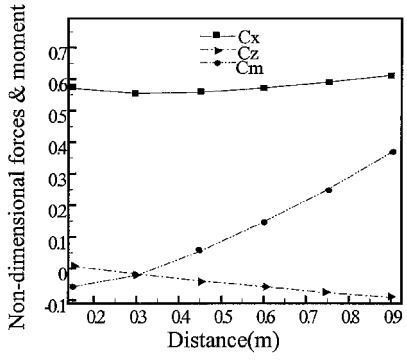

Fig. 14a Aerodynamic forces and moment at various distances of booster.

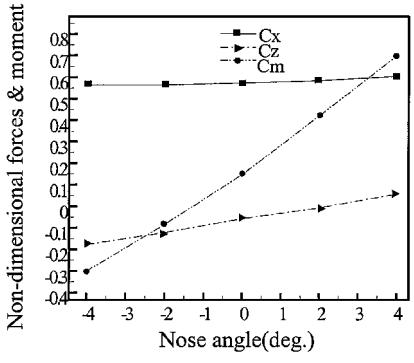

Fig. 14b Aerodynamic forces and moment at various nose angles of booster.

around the bodies are shown at every 0.1 s after free body separation. From the design of KSR-III, the initial distance between the core rocket and booster is set to 0.15 m. The booster falls with a negative pitching motion. Because this slight negative pitching motion might increase the negative pitching moment of the booster as mentioned in the preceding attitude analyses, the upside collision is inevitable during the separation stages. Thus additional jettisoning forces and moments are necessary for a safe separation of booster.

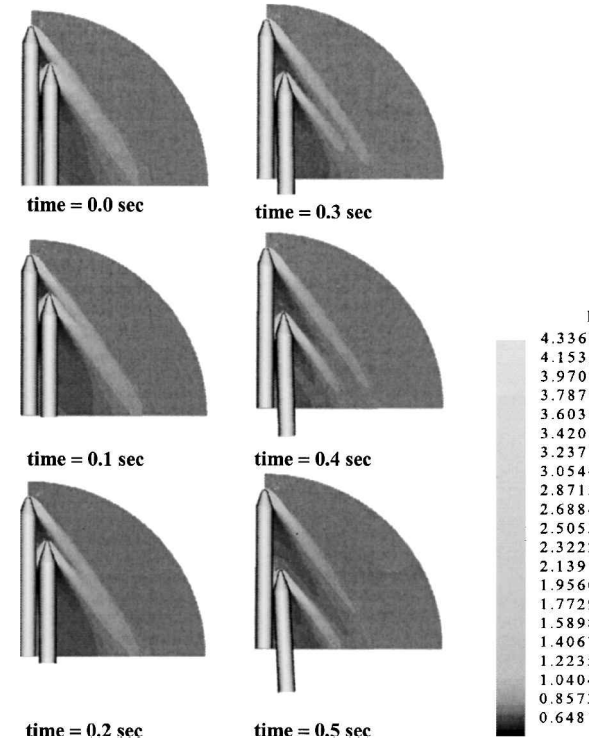

Fig. 15 Booster trajectory of KSR-III with pressure contours (free separation, no jettisoning force and moment).

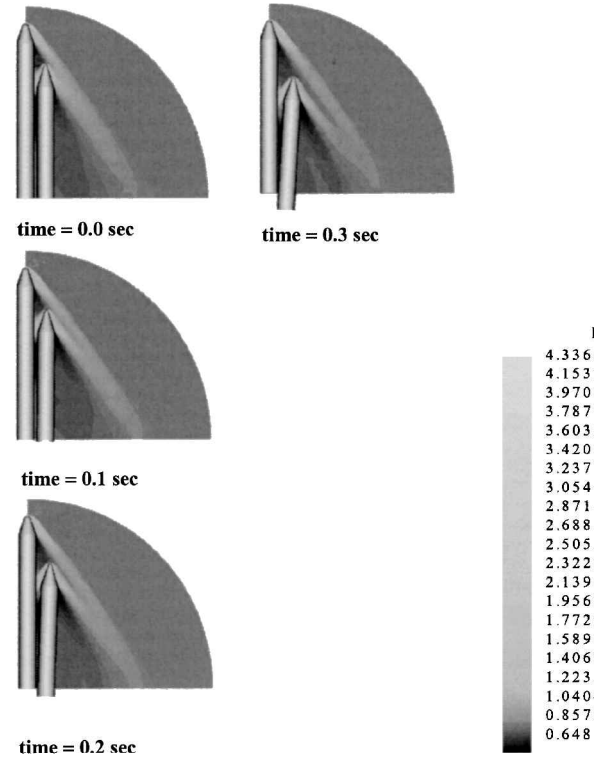

Fig. 16 Booster trajectory of KSR-III with pressure contours (nondimensional jettisoning moment = 0.356).

Figure 16 shows the booster trajectory and pressure contour around the vehicle when the nondimensional jettisoning moment of 0.356 acts on the booster. In this case the booster hits the downside of the core rocket after 0.4 s of its separation as a result of excessive jettisoning moment. This result suggests that some restrictions of jettisoning moments are desired to avoid collision. Numerous forced separation cases were simulated with various combination of jettisoning forces and moments. Figure 17 shows the map of jettisoning forces and moments necessary for the safe separation of

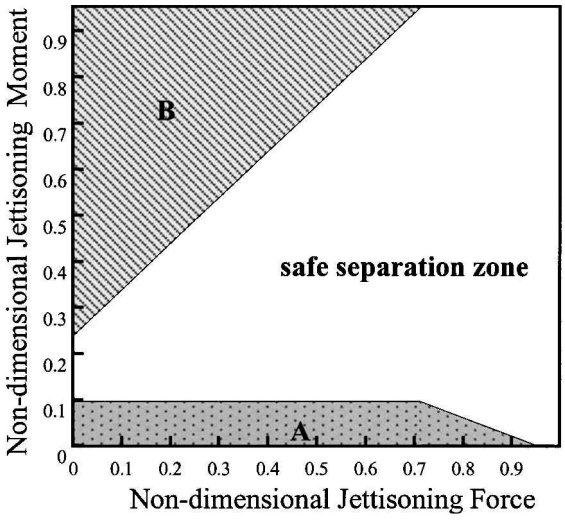

Fig. 17 Guideline map of jettisoning force and moment for KSR-III.

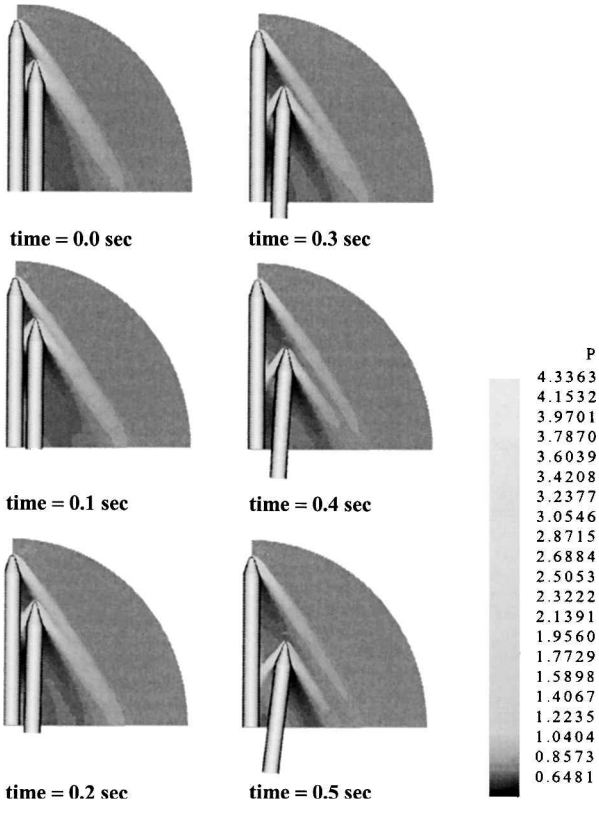

Fig. 18 Booster trajectory of KSR-III with pressure contours (nondimensional jettisoning force = 0.475, jettisoning moment = 0.238).

the booster obtained from the computations. Region A represents the upside collision zone where the upside of booster hits the core during the separation stages by the negative aerodynamic pitching moment. In this region collision occurs even with a large jettisoning force because the jettisoning moment is not enough to overcome the negative pitching motion of booster. Region B represents the downside collision zone where the excessive jettisoning moment causes too large positive pitching motion of the booster. Figure 18 shows an example of safe separation when the nondimensional jettisoning force of 0.475 and moment of 0.238 act on the booster.

Conclusions

An efficient three-dimensional aerodynamic-dynamic coupled code is developed to simulate the separation dynamics of strap-on boosters in the dense atmosphere. The chimera overset grid technique is used for the multibody dynamic motion, and a domain division technique is implemented in order to reduce the computational cost required to find interpolation points in the chimera grids. The trajectories of the separated boosters are then predicted for the H-II launch vehicle and the KSR-III sounding rocket. From the analyses it is observed that vehicles with large strap-ons can produce more complex flowfield characteristics. Collisions of bodies during the separation stages might result if the attitudes of boosters are not properly controlled. A guideline map of jettisoning force and moment guaranteeing the safe separation has been generated for the KSR-III using the computational approach, demonstrating the utility of the technique.

Acknowledgments

The authors would like to thank the Korea Aerospace Research Institute and the Brain Korea 21 Project for financial support.

References

[1]Meakin, R. L., and Suhs, N. E., "Unsteady Aerodynamic Simulation of Multiple Bodies in Relative Motion," AIAA Paper 89-1996, June 1989.

[2]Lochan, R., and Adimurthy, V., "Separation Dynamics of Strap-On Boosters in the Atmosphere," *Journal of Guidance, Control, and Dynamics*, Vol. 20, No. 4, 1997, pp. 633–639.

[3]Lijewski, L. E., and Suhs, N. E., "Time-Accurate Computational Fluid Dynamics Approach to Transonic Store Separation Trajectory Prediction," *Journal of Aircraft*, Vol. 31, No. 4, 1994, pp. 521–526.

[4]Palmer, G., and Buning, P., "Three-Dimensional Computational Analysis of Complex Launch Vehicle Configurations," *Journal of Spacecraft and Rockets,* Vol. 33, No. 1, 1996, pp. 49–53.

[5]Taylor, S., and Wang, J. C. T., "Launch-Vehicle Simulations Using a Concurrent, Implicit Navier–Stokes Solver," *Journal of Spacecraft and Rockets,* Vol. 33, No. 5, 1996, pp. 601–606.

[6]Azevedo, J. L. F., and Moraes, P., Jr., "Code Validation for High-Speed Flow Simulation Over Satellite Launch Vehicle," *Journal of Spacecraft and Rockets*, Vol. 33, No. 1, 1996, pp. 15–21.

[7]Baldwin, B. S., and Lomax, H., "Thin Layer Approximation and Algebraic Model for Separated Turbulent Flows," AIAA Paper 78-257, Jan. 1978.

[8]Degani, D., and Schiff, L. B., "Computation of Turbulence Supersonic Flows Around Pointed Bodies Having Crossflow Separation," *Journal of Computational Physics*, Vol. 66, No. 1, 1986, pp. 173–196.

[9]Yoon, S., and Jameson, A., "Lower-Upper Symmetric–Gauss-Seidel Method for the Euler and Navier–Stokes Equations," *AIAA Journal*, Vol. 26, No. 9, 1988, pp. 1025, 1026.

[10]Kim, K. H., Kim, C., and Rho, O. H., "Accurate Computations of Hypersonic Flows Using AUSMPW+ Scheme and Shock-Aligned-Grid Technique," AIAA Paper 98-2442, Jan. 1998.

[11]Van Leer, B., "Towards the Ultimate Conservative Difference Scheme. V. A Second Order Sequel to Godunov's Methods," *Journal of Computational Physics*, Vol. 32, No. 2, 1979, pp. 101–136.

[12]Anderson, W. K., Thomas, J. L., and Van Leer, B., "Comparison of Finite Volume Flux Vector Splittings for the Euler Equations," *AIAA Journal*, Vol. 24, No. 9, 1986, pp. 1453–1460.

[13]Steger, J. L., Dougherty, F. C., and Benek, J. A., "A Chimera Grid Scheme," *Advances in Grid Generation*, FED Vol. 5, edited by K. N. Ghia, American Society of Mechanical Engineers, New York, 1983, pp. 59–69.

[14]Meakin, R. L., "On the Spatial and Temporal Accuracy of Overset Grid Methods for Moving Body Problem," AIAA Paper 94-1925, June 1994.

P. Weinacht
Associate Editor